



**HAL**  
open science

## Selenium Nanowire Formation by Reacting Selenate with Magnetite

Agnieszka Poulain, Alejandro Fernandez-Martinez, Jean-Marc Greneche, Damien Prieur, Andreas Scheinost, Nicolas Menguy, Sarah Bureau, Valérie Magnin, Nathaniel Findling, Jakub Drnec, et al.

► **To cite this version:**

Agnieszka Poulain, Alejandro Fernandez-Martinez, Jean-Marc Greneche, Damien Prieur, Andreas Scheinost, et al.. Selenium Nanowire Formation by Reacting Selenate with Magnetite. *Environmental Science and Technology*, 2022, 56 (20), pp.14817-14827. 10.1021/acs.est.1c08377 . hal-03872307

**HAL Id: hal-03872307**

**<https://hal.science/hal-03872307>**

Submitted on 25 Nov 2022

**HAL** is a multi-disciplinary open access archive for the deposit and dissemination of scientific research documents, whether they are published or not. The documents may come from teaching and research institutions in France or abroad, or from public or private research centers.

L'archive ouverte pluridisciplinaire **HAL**, est destinée au dépôt et à la diffusion de documents scientifiques de niveau recherche, publiés ou non, émanant des établissements d'enseignement et de recherche français ou étrangers, des laboratoires publics ou privés.

# Selenium nanowire formation by reacting selenate with magnetite

*Agnieszka Poulain<sup>1</sup>, Alejandro Fernandez-Martinez<sup>1\*</sup>, Jean-Marc Greneche<sup>2</sup>, Damien Prieur<sup>3</sup>,  
Andreas C. Scheinost<sup>3</sup>, Nicolas Menguy<sup>4</sup>, Sarah Bureau<sup>1</sup>, Valérie Magnin<sup>1</sup>, Nathaniel Findling<sup>1</sup>,  
Jakub Drnec<sup>5</sup>, Isaac Martens<sup>5</sup>, Marta Mirolo<sup>5</sup>, Laurent Charlet<sup>1\*</sup>*

<sup>1</sup> Univ. Grenoble Alpes, Univ. Savoie Mont Blanc, CNRS, IRD, IFSTTAR, ISTERre, 38000  
Grenoble, France

<sup>2</sup> Institut des Molécules et Matériaux du Mans, CNRS UMR-6283, Le Mans Université, Le  
Mans, F-72085, France.

<sup>3</sup> The Rossendorf Beamline at ESRF, 71 avenue des Martyrs, 38043 Grenoble, France, and  
HZDR Institute of Resource Ecology, Bautzener Landstrasse 400, 01328 Dresden, Germany

<sup>4</sup> Sorbonne Université, Muséum National d'Histoire Naturelle, UMR CNRS 7590, IRD. Institut  
de Minéralogie, de Physique des Matériaux et de Cosmochimie (IMPMC), 4 Place Jussieu,  
75005, Paris, France

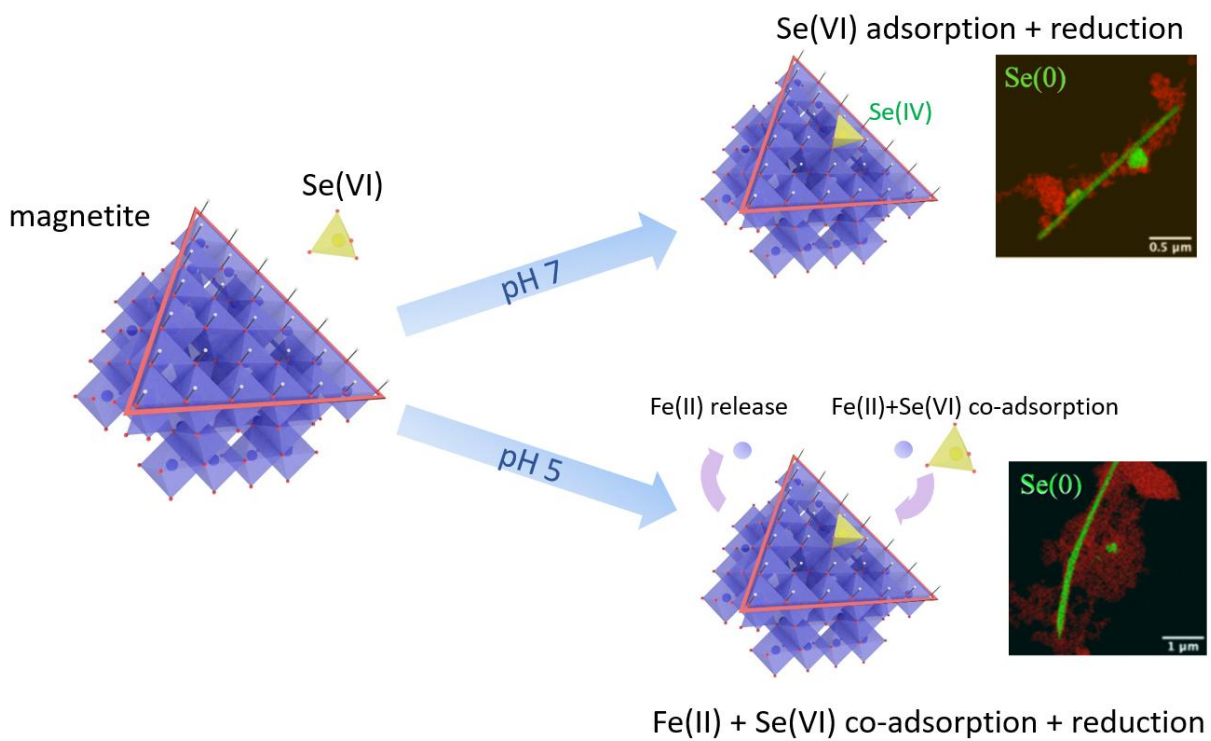
<sup>5</sup> ESRF, 71 avenue des Martyrs, 38043 Grenoble, France

\* [Alex.Fernandez-Martinez@univ-grenoble-alpes.fr](mailto:Alex.Fernandez-Martinez@univ-grenoble-alpes.fr); [Laurent.Charlet@univ-grenoble-alpes.fr](mailto:Laurent.Charlet@univ-grenoble-alpes.fr)

KEYWORDS: Nuclear wastes, Selenium reduction, Sorption on magnetite, Selenium needles,  
Magnetite to maghemite interconversion

## SYNOPSIS

Studies of selenate reduction on magnetite at neutral and acidic pH revealing different retention  
mechanisms.



30 **ABSTRACT**

31 The mobility of  $^{79}\text{Se}$ , a fission product of  $^{235}\text{U}$  and long-lived radioisotope, is an important  
32 parameter in the safety assessment of radioactive nuclear waste disposal systems. Non-  
33 radioactive selenium is also an important contaminant of drainage waters from black shale  
34 mountains and coal mines. Highly mobile and soluble in its high oxidation states, selenate  
35 ( $\text{Se(VI)O}_4^{2-}$ ) and selenite ( $\text{Se(IV)O}_3^{2-}$ ) oxyanions can interact with magnetite, a mineral present  
36 in anoxic natural environments and in steel corrosion products, thereby being reduced and  
37 consequently immobilized by forming low-solubility solids. Here, we investigated the sorption  
38 and reduction capacity of synthetic nanomagnetite towards Se(VI) at neutral and acidic pH,  
39 under reducing, oxygen-free conditions. The additional presence of  $\text{Fe(II)}_{\text{aq}}$ , released during  
40 magnetite dissolution at pH 5, has an effect on the reduction kinetics. X-ray absorption  
41 spectroscopy analyses revealed that, at pH 5, trigonal gray Se(0) formed, and that sorbed Se(IV)  
42 complexes remained on the nanoparticle surface during longer reaction times. The Se(0)  
43 nanowires grew during the reaction, which points to a complex transport mechanism of reduced  
44 species or to active reduction sites at the tip of the Se(0) nanowires. The concomitant uptake of  
45 aqueous Fe(II) and Se(VI) ions is interpreted as a consequence of small pH oscillations that  
46 result from the Se(VI) reduction, leading to a re-adsorption of aqueous Fe(II) onto the magnetite,  
47 renewing its reducing capacity. This effect is not observed at pH 7, where we observed only the  
48 formation of Se(0) with slow kinetics due to the formation of an oxidized maghemite layer. This  
49 indicates that the presence of aqueous Fe(II) may be an important factor to be considered when  
50 examining the environmental reactivity of magnetite.

51

52

## 53 INTRODUCTION

54 Selenium is an essential micronutrient often called ‘double-edged sword element’<sup>1</sup> or ‘essential  
55 toxin’,<sup>2</sup> due to one of the narrowest tolerance limits in the periodic table (40 and 400 µg/day).<sup>3,4</sup>  
56 Aqueous species of selenium show – similar to sulfur - a variety of oxidation states, the  
57 distribution of which depends strongly on the environmental conditions. Selenate (Se(VI)O<sub>4</sub><sup>2-</sup>)  
58 and selenite (Se(IV)O<sub>3</sub><sup>2-</sup>) are water-soluble species which account for 95% of selenium toxicity  
59 related to accumulation in plant and animal tissues,<sup>3</sup> reflecting its concentration and  
60 bioavailability in soil. Se(VI) predominates at high redox potential and under alkaline conditions  
61 and has a low adsorption and precipitation ability, while Se(IV) occurs at moderate redox  
62 potentials and its mobility is mainly governed by sorption/desorption processes.<sup>4</sup> Elemental  
63 selenium [Se(0)], metal selenides [Se(-II) and Se(-I)], and selenium sulfides are essentially  
64 insoluble and are therefore considered immobile in soil and geologic systems. Quantifying the  
65 rates and thermodynamic conditions of selenium reduction is therefore important to assess the  
66 mobility of selenium in the environment.<sup>5</sup>

67 The <sup>79</sup>Se radioisotope (half-life 2.95 x 10<sup>5</sup> years) is a <sup>235</sup>U fission product. Although the main  
68 oxidation state of selenium in radioactive waste has been reported to be Se(-II),<sup>6</sup> understanding  
69 the redox reactivity and geochemical cycling of oxidized species of selenium (selenate and  
70 selenite) in the environment is necessary to assess the impact of an eventual release of waste  
71 repositories to the biosphere, or the eventual breach of natural –oxygenated– waters into the  
72 repository.<sup>7</sup> Among all the cementitious materials in engineered barriers and all the naturally  
73 occurring minerals in the surrounding geologic formations, only a few have the ability to uptake  
74 selenium oxyanions via either adsorption processes or reductive precipitation. These are, e.g.,  
75 layered double hydroxides such as the hydrotalcite phases in cements (AFm),<sup>8</sup> and the redox  
76 active Fe(II)-bearing phases present as the result of corrosion of the steel containers or naturally  
77 in minerals such as pyrite, mackinawite, magnetite or Fe(II)-bearing clay minerals.<sup>9–17</sup> Abiotic  
78 reduction of soluble selenium species by Fe(II)-bearing materials (potential steel corrosion  
79 products) has been observed for several minerals such as green rust,<sup>18–20</sup> magnetite,<sup>15,21,22</sup>  
80 mackinawite and siderite,<sup>15</sup> pyrite,<sup>23,24</sup> troillite<sup>25</sup> and zero-valent iron.<sup>26</sup> The mixed-valence  
81 Fe(II)/(III) oxide magnetite (Fe<sub>3</sub>O<sub>4</sub>) has showed redox reactivity towards selenium species.<sup>15,21,22</sup>  
82 Magnetite nanoparticles have been shown to reduce Se(IV) and Se(VI) to elemental selenium

83 and iron selenides<sup>15,27</sup>, even in the presence of oxidized layers or maghemite and coatings.<sup>21,28</sup>  
84 The product of these redox processes is a partially oxidized magnetite, i.e. a magnetite particle  
85 containing some proportion of maghemite –a Fe(III) mineral isostructural to magnetite, a phase  
86 that is also able to adsorb selenium oxyanions.<sup>11,28</sup>

87 Despite the high number of studies dealing with selenium redox reactivity in the presence of  
88 Fe(II) redox active phases, some important questions remain open about the mechanism of  
89 selenium reduction by magnetite and the growth of the reduced selenium phases. For example: is  
90 electron transfer possible when the complex formed are outer-sphere? Whereas selenite is prone  
91 to form inner-sphere complexes at the magnetite-water interface,<sup>21,28–30</sup> selenate oxyanions  
92 adsorb forming outer-sphere complexes.<sup>22,28</sup> However, it has been shown that electron transfer  
93 can still take place, with a selenite intermediate formed, and the whole reaction showing slow  
94 reduction kinetics indicative of a redox process with high kinetic barriers.<sup>21</sup> Fe(II) ions are also  
95 known to be released from magnetite to solution at acidic pH, acting as a reactive species that  
96 can re-adsorb and donate electrons thereby reducing adsorbed ions such as arsenate.<sup>31–34</sup> Are  
97 these processes active in the presence of selenium ions as well? Accounting for the presence of  
98 Fe(II) is mandatory for geochemical models used to predict the fate of radionuclides in systems  
99 for nuclear waste storage. To date, no systematic study has been performed that describes the  
100 redox interactions of selenium oxyanions with magnetite in the presence of Fe(II).

101 Here, a combination of spectroscopy and wet chemistry techniques are used to evaluate the  
102 relevance of Fe(II) during the reduction process of selenate at the magnetite-water interface, and  
103 to characterize the mechanisms of selenite reduction and its reduction products, giving  
104 molecular-scale insight into the mechanisms of formation of reduced selenium phases.

105

## 106 **MATERIALS AND METHODS**

107 All solutions were prepared with boiled, nitrogen-degassed Millipore 18.2 M $\Omega$  water. Reagent  
108 grade NaOH ( $\geq 98\%$ , Sigma Aldrich) and HCl (37%, Carl Roth) were used for preparation of 1 M  
109 and 0.1 M stock solutions for pH control. A SENTRON pH meter was calibrated with VWR  
110 buffers, and a Pt redox electrode for Eh measurements with a 200 mV buffer solution. All  
111 experiments and synthesis were conducted at room temperature in an Ar-filled Jacomex

112 glovebox, with a controlled oxygen partial pressure ( $[O_2] < 2$  ppm), using closed vials to contain  
113 all the solution.

#### 114 **Magnetite synthesis and characterization**

115 Magnetite was synthesized following the protocol of Jolivet et al.<sup>35</sup> by slowly adding 60 ml of 6  
116 M  $NH_3$  (Sigma Aldrich) to 50 ml solution containing  $[Fe_{tot}] = 0.55$  M and  $[Fe(II)]/[Fe(III)] = 0.5$ ,  
117 prepared by adding 0.4 M  $FeCl_2$  (tetrahydrate, Sigma Aldrich) to 0.8 M  $FeCl_3$  (hexahydrate,  
118 Merck). The solution turned black immediately upon mixing and was left for 24 h on a rotary  
119 shaker. Afterwards a strong magnet was used to separate the magnetic particles and the  
120 supernatant was filtered (0.22  $\mu m$  MF-Millipore). The magnetite was rinsed 4 times with water  
121 and 2 times with 0.1 mM NaCl solution, the latter one also used for its storage.

122 **XRD.** Samples were loaded inside the glove box into kapton capillaries, sealed with epoxy glue  
123 and stored in anoxic conditions until measurement. X-ray powder diffraction data were collected  
124 at room temperature at the ID31 beamline at the ESRF ( $\lambda = 0.1907$  Å) using a Pilatus3 X CdTe  
125 2M detector with 172  $\mu m \times 172$   $\mu m$  pixel size. The detector was calibrated using the NIST  
126 certified  $CeO_2$  674b standard. Azimuthal integrations were performed using the pyFAI  
127 package.<sup>36</sup> The lattice parameters, average crystallite sizes using the Debye-Scherrer equation,  
128 and phase fractions were determined using Rietveld analysis with the FullProf Suite.<sup>37</sup> The  
129 advantages of synchrotron over laboratory X-ray source are: a better signal to noise ratio thanks  
130 to high photon flux and a noise-free detector (Figure S1), faster measurements (few seconds vs  
131 few hours) and the smaller amount of powder required (beneficial for small-scale sorption  
132 experiments).

133 **BET.** The specific surface area (SSA) was determined by the Brunauer–Emmett–Teller  
134 adsorption method (BET- $N_2$ ) at 77 K, using a Belsorp-Max (Bel Japan) volumetric gas sorption  
135 instrument. A small amount (0.418 g) of magnetite was loaded in a glass cell inside the glovebox  
136 and then dried under vacuum at 80 °C during 12 h. The SSA was calculated from the BET  
137 equation in the  $P/P_0$  range 0.052-0.307.

138  **$^{57}Fe$  Mössbauer.** The spectra were collected at 300 and 77 K using a conventional constant  
139 acceleration transmission spectrometer with a  $^{57}Co$ (Rh) source and an  $\alpha$ -Fe foil as calibration  
140 sample. To obtain 5 mg  $Fe/cm^2$  to satisfy the fine absorber conditions, 20 mg of the powder was

141 loaded inside the glovebox in flat round plastic holders, sealed with epoxy glue, and transported  
142 in oxygen free conditions. Then the hyperfine structure was modeled by means of quadrupole  
143 doublets and/or magnetic sextets with Lorentzian lines using the homemade program MOSFIT.<sup>38</sup>

144 **Transmission Electron Microscopy (TEM).** A few milligrams of solid samples were placed in  
145 plastic tubes, filled with 10 mL of ethanol (previously stored for several weeks in the glovebox),  
146 sealed with parafilm, and removed from the glovebox for 5 minutes for redistribution in an  
147 ultrasonic bath. Next, the solutions were immediately transferred back to the glovebox, diluted  
148 with ethanol and drop-casted on pure carbon, 200 mesh Cu TEM grids (TED PELLA, INC.). The  
149 samples were transferred to the microscope in anoxic conditions and were in contact with air  
150 only for few minutes during mounting on the microscope sample holder. Conventional  
151 Transmission Electron Microscopy (TEM), High Angular Angle Dark Field imaging in scanning  
152 mode (STEM-HAADF), X-ray Energy-Dispersive Spectroscopy (XEDS) and Selected Area  
153 Electron Diffraction (SAED) patterns were collected at IMPMC, Sorbonne University, Paris,  
154 using a JEOL 2100F microscope. Fast Fourier Transform on HR TEM images were carried out  
155 using ImageJ software<sup>39</sup> and SAED pattern were indexed using SingleCrystal Software.<sup>40</sup>

156 **Batch sorption experiments.** Sorption experiments of selenate on magnetite were performed in  
157 glass bottles at room temperature in an Ar-filled glovebox. All selenate solutions were prepared  
158 from Na<sub>2</sub>SeO<sub>4</sub> (BioXtra, Sigma-Aldrich®). The concentration of dry magnetite in four 100 mL  
159 batches was fixed at 10 g/L in 0.1 mM NaCl background electrolyte. Due to stronger selenium  
160 adsorption on magnetite in acidic conditions,<sup>21</sup> pH 5 and 7 were selected for comparison. The  
161 acidity of the initial suspensions was adjusted during 96 h by adding drops of 0.1 M HCl or  
162 NaOH stock solutions, until the pH was not drifting from the desired value by more than 0.2 unit  
163 within 24h. After this equilibration step, aliquots of Se(VI) stock solution were added to obtain  
164 the total target concentration of 8.6 mM (details in Table S1). This should cover 100% of the [-  
165 Fe-OH] surface reactive sites, as calculated from the BET-determined specific surface area  
166 values and the theoretical crystallographic site density of magnetite, 8 sites/nm<sup>2</sup>.<sup>41</sup>

167 In the absence of the values of real concentrations of selenate in the underground repositories,  
168 the concentration of selenium was chosen so (i) the solutions are undersaturated with respect to  
169 any Fe(II)-Se(IV) phases, and so they are high enough to be observed via the physico-chemical  
170 characterization tools used here.

171 The addition of Se(VI) to the magnetite suspension stabilized at pH 5 resulted in an increase of  
172 the pH to 5.4, which was immediately readjusted to pH 5.0. No change of pH was observed upon  
173 addition of Se(VI) to the magnetite suspension stabilized at pH 7. The pH of the suspensions was  
174 monitored and readjusted, if necessary, throughout the experiment. This addition of acid did not  
175 modify significantly the solid-to-liquid ration of the reaction (less than 1%). The two reactors  
176 were placed on a rotary shaker and 5 mL aliquots of the suspension were sampled at selected  
177 time intervals. The solid was isolated by magnetic separation, dried using a vacuum filtration  
178 system (0.22  $\mu\text{m}$ ), and used for further X-ray Absorption Spectroscopy (XAS) and Mössbauer  
179 spectroscopy, TEM, XRD characterization. The liquid was filtered through a syringe filter (0.22  
180  $\mu\text{m}$ ) and used for ICP-AES, IC and Eh analyses.

181 **ICP-AES and IC.** The total concentrations of Se in the liquid samples were determined after  
182 dilution by ICP-AES (Varian 720ES, detection range 0.05 - 50 ppm), while the concentrations of  
183 Se(VI) and Se(IV) were determined by Ion Chromatography (Dionex Inegriion HPIC, Thermo  
184 Scientific, detection range 0.1 - 10 ppm). The difference between the initial selenium  
185 concentration ( $c_0$ ) and the measured value ( $c_e$ ) provided the amount of adsorbed species.

186 **XAS.** Pelletized samples (BN filler) were flash-frozen and stored until measurement in a liquid  
187 nitrogen Dewar to stop the chemical reaction after the predefined time intervals and to prevent  
188 any oxygen-induced oxidation. X-ray absorption spectra (both X-ray Absorption Near Edge  
189 Structure and Extended X-ray Absorption Fine Structure) were collected at the Rossendorf  
190 Beamline (BM20)<sup>42</sup> at the ESRF, at the Se-K edge (12 657 eV), using a pair of Rh-coated  
191 mirrors for collimation and suppression of higher harmonics. The energy of the Si(111)  
192 monochromator was calibrated using an Au foil at L3 edge (11 918 keV). Fluorescence spectra  
193 were acquired with an 18-element solid-state Germanium detector (Ultra-LEGe, GUL0055,  
194 Mirion Technologies). Several spectra were measured to obtain sufficient signal quality, with the  
195 number of total spectra averaged per each sample varying from 1 to 10 depending on the  
196 concentration of Se. Measurements were conducted at 15 K using a closed-cycle He cryostat, to  
197 avoid photon-induced redox reactions and to exclude thermal disorder. Energy calibration and  
198 merging of individual scans was performed with SixPack,<sup>43</sup> normalization and all other data  
199 treatment steps were done with WinXAS.<sup>44</sup> Both XANES and EXAFS spectra were used to  
200 derive the number of spectral components, to identify them and to determine their fractions in

201 individual samples, by employing the ITFA package,<sup>45,46</sup> and using spectra of selected,  
202 previously published selenium standards (aqueous selenite, aqueous selenate, gray Se(0), red  
203 Se(0), ferroselite).<sup>15,27,47</sup>

204

## 205 **RESULTS AND DISCUSSION**

206 Magnetite nanoparticles were characterized after synthesis via XRD, Mössbauer spectrometry  
207 and TEM. An average crystallite size of 15 nm was estimated using the Scherrer equation, while  
208 TEM image showed rather large distribution of particles ranging from 5 to 50 nm, aggregated in  
209 large clusters. More information is shown in the supporting information.

### 210 **Se(VI) sorption kinetics experiments on magnetite at pH 5 and 7**

211 Results of the Se(VI) sorption experiments at pH 5 and 7 are given in Figure 1 and Table S2.

212 **Se(VI)** uptake was fastest during the first 240 h in the two experimental series, with the rate  
213 depending on the solution pH, as already observed previously.<sup>22,48</sup> During this time, 43% of the  
214 selenate was removed from the solution at pH 5, in contrast with only 22% removed at pH 7. The  
215 uptake stagnated after ~1000 h for both pH values.

216 After the first 240 h, a plateau (within analytical error) was observed at pH 7, which would  
217 correspond to about 1.5 Se(VI) molecules/nm<sup>2</sup>. At pH 5 the removal process continued but at a  
218 much lower rate, reaching 53% after 3600 h, equivalent to about 4.2 Se(VI) molecules/nm<sup>2</sup>. This  
219 indicates that the theoretical sorption capacity (8 sites/nm<sup>2</sup>) calculated for [Fe-OH] groups on the  
220 {111} crystallographic faces of magnetite<sup>41</sup> was only partially reached, with a level of 53% at pH  
221 5, and 22% at pH 7. On the other hand, and as described in a previous study for selenite,<sup>28</sup> if  
222 inner sphere complexes with bidentate ligands are formed, these would account for 8.4 Se(VI)  
223 molecules/nm<sup>2</sup>, a value very close to the theoretical site density.

224 ICP-AES results were confirmed by IC measurements, which can distinguish the two soluble  
225 forms, Se(IV) and Se(VI). The reduced, soluble selenite oxyanion [Se(IV)O<sub>3</sub><sup>2-</sup>] remained below  
226 the detection limit at both pH values, suggesting any eventual reduction process would take place  
227 at the mineral surface and not in solution during the 3600 h of the reaction. However, due to the

228 necessary sample dilution (the IC upper detection limit for Se(VI) is  $\sim 0.13$  mmol/L), low  
229 concentrations of selenite might remain undetectable.

230 If no reduction occurred, we could have assumed that the negatively charged oxyanions were  
231 exclusively adsorbed via electrostatic attraction to the positively charged surface sites of  
232 magnetite or maghemite, below their isoelectric points ( $\text{IEP}_{\text{magnetite}} = 6.4\text{-}8$ ,  $\text{IEP}_{\text{maghemite}} = 5.5\text{-}$   
233  $7.5$ ),<sup>48</sup> as found for selenate and selenite adsorbed on positively charged  $\text{FeOH}_2^+$  groups of  
234 maghemite.<sup>11,12</sup>

### 235 **Aqueous Fe(II)**

236 At pH 7, the concentration of  $\text{Fe(II)}_{\text{aq}}$  stayed below 0.01 mmol/L during 4000 h, so we could  
237 assume that the magnetite was fairly pure at  $t_0$  (as confirmed by Mössbauer spectrometry).

238 At pH 5, after injection of selenate and throughout the 4000 h of the sorption experiments, a re-  
239 adsorption of the  $\text{Fe(II)}$  was observed, with an initial value of 1.87 mmol/L measured after 0.17 h  
240 of reaction and a practical depletion from the solution after  $\sim 1000$  h, time at which the selenate  
241 removal was observed to stagnate as well (see Figures 1 and 4). While the re-adsorption of  
242  $\text{Fe(II)}_{\text{aq}}$  on magnetite is not favored at pH 5 due to the positively charged mineral surface,<sup>31,33</sup> the  
243 presence of  $\text{Fe(II)}_{\text{aq}}$  may catalyze changes in the chemistry of Se(VI), via the formation of  
244 ternary surface complexes. To test this hypothesis a linear plot was performed, that reveals  
245 indeed a co-removal dependency between Se(VI) and  $\text{Fe(II)}_{\text{aq}}$  (Figure 1b). The slope of the curve  
246 indicates that  $\sim 0.5$  mol of Fe(II) is removed from solution per one mol of Se(VI). The initial ratio  
247  $n\text{Fe(II)}_{\text{aq}}/n\text{Se(VI)}_{\text{aq}}$  in the solution was 0.3:1. Note that a reduction of selenate to selenite by the  
248 oxidation of Fe(II) to Fe(III) would require a ratio of 2:1 (and even higher for reductions of  
249 selenite to Se(0) or Se(-II)), so the observed value of 0.5:1 points to a completely different,  
250 secondary process involving the solid phase. Extrapolation of the co-removal results allowed the  
251 estimation of an initial aqueous iron concentration at  $t_0$  equal to 2.4 mmol/L, corresponding to  
252 the 5.6% of maghemite initially present (before selenate injection). This corresponds to about  
253 one monolayer of maghemite for the averaged 15 nm diameter spherical particles, so that  
254 electron exchange between the surface and the core of the magnetite should still be possible.

255 Several studies have shown that reduction of environmental contaminants is effectively catalyzed  
256 by  $\text{Fe(II)}_{\text{aq}}$  adsorbed on magnetite,<sup>32,49</sup> montmorillonite,<sup>47</sup> goethite and lepidocrocite<sup>50</sup> and zero-

257 valent iron.<sup>51</sup> Examination of the reduction of selenate by ZVI<sup>51</sup> and the removal of arsenic by  
258 non-stoichiometric magnetite<sup>33</sup> demonstrated the importance of the initial Fe(II)<sub>aq</sub> concentration  
259 on the extent of pollutant reduction. Aqueous Fe(II)<sub>aq</sub> alone, however, did not show significant  
260 Se(VI) reduction.<sup>51</sup>

## 261 **Mineral transformation – Mössbauer and XRD**

262 Magnetite to maghemite transformation was revealed by both <sup>57</sup>Fe Mössbauer spectrometry and  
263 X-ray diffraction (Figure S6). In the Rietveld refinement process only little freedom was given to  
264 the magnetite and maghemite unit cell parameters (a +/- 0.005 Å) to avoid erroneous phase  
265 identification. Analysis of the selected solid samples showed a large correlation between the two  
266 techniques (Table S3 and Figure 2) at pH 5, where a significant degree of transformation  
267 occurred, while at pH 7 XRD gives a smaller maghemite percentage in comparison to that  
268 estimated by Mössbauer spectrometry. A shift of the XRD peaks related to mineral  
269 transformation at pH 5 between 6 h and 4032 h is clearly visible in Figure S6b, especially at the  
270 higher angles, while at pH 7 (Figure S6d) the corresponding higher angle peaks tend to be  
271 superimposed. This could indicate that at pH 7 the low maghemite fraction is not significantly  
272 disturbing the magnetite crystal lattice (randomly distributed Fe<sup>3+</sup> cations), or that the thin  
273 oxidized layer at the mineral surface is amorphous, thus not contributing to the Bragg peaks and  
274 only to diffuse scattering.

275 Another important observation is the strong correlation between the degree of magnetite  
276 oxidation (as expressed by Fe(II) solubility) and the Se(VI) uptake, as highlighted in Figure 2. At  
277 pH 7, 18% of maghemite (Mössbauer) formed during the first 6 hours, concomitantly with 1.27  
278 mmol/L of Se(VI) removed from solution, which corresponds to 1% of mineral conversion, or  
279 0.43 mmol/L of maghemite produced following equation S1, for every 0.07 mmol/L uptake of  
280 Se(VI). Between 6 h and 2280 h the conversion rate slowed down to 0.035 mmol/L of Se(VI) for  
281 each 1% of mineral, probably due to partial oxidation of the magnetite surface which blocked the  
282 electron transfer.<sup>52</sup>

283 A detailed analysis of the XRD patterns revealed a new peak corresponding to the (100) plane of  
284 trigonal gray Se(0)<sup>53</sup> at 2.9 ° ( $\lambda = 0.1907$  Å, Figure S6c), which increased concomitantly with  
285 the Se(VI) uptake and the mineral transformation (1% of Se(0) after 3600 h at pH 7). The redox

286 process describing the Se(VI) reduction to Se(0) and magnetite oxidation, with an exchange of 6  
287 electrons can be written as:



289 Based on this model equation, with the initial magnetite concentration fixed at 10 g/L, 0.1 g of  
290 maghemite (1% phase fraction or ~0.43 mmol/L of maghemite produced) should appear after  
291 reduction of 0.07 mM of selenate oxyanion by magnetite (details of calculation in SI). At the  
292 same time, consumption of protons should increase the pH of the solution, as observed in all  
293 batch experiments. This ideal stoichiometry was only observed in the initial phase of the Se(VI)  
294 experiment at pH 7. While selenate was still available in the solution (6.5-7 mmol/L) after ~2500  
295 h of the reaction, the limiting factor, which slows down the adsorption, must be the access to  
296 reducing magnetite sites.

297 Magnetite reacting at pH 5 with Se(VI) for 4032 h resulted in about 3.4% of Se(0) (XRD fitting),  
298 but the main redox reaction describing the process in equation 1 is more complicated, because of  
299 the presence of  $\text{Fe}(\text{II})_{\text{aq}}$  leading to a secondary reaction. In the combined magnetite/ $\text{Fe}(\text{II})_{\text{aq}}$   
300 system, the electrons migrate within the bulk and across the solid water interface.<sup>31</sup> The partially  
301 oxidized, positively charged magnetite surface can adsorb negatively charged selenate and  
302 selenite,<sup>12,35</sup> but the magnetite surface is also renewed via  $\text{Fe}(\text{II})_{\text{aq}}$ .

303 The estimated initial maghemite fraction at pH 5, before Se(VI) injection, was equal to 5.6%,  
304 and increased to 24% after 6 h. At the same time 1.55 mmol/L of selenate was removed from the  
305 solutions. This corresponds to a selenate concentration decrease of 0.084 mmol/L for each 1% of  
306 oxidized mineral (after subtraction of the maghemite present initially in the solid), thus more  
307 than the  $[\text{Se}(\text{VI})]$  decrease estimated from equation 1. In the following 2280 h, the selenate  
308 removal rate dropped down to 0.07 mmol/L per 1% of mineral transformation. If we compare the  
309 whole period of 2280 h for the experiments at both pH, without subtraction of the initial  
310 maghemite due to acidic dissolution, the same Se(VI) removal – mineral oxidation ratio is found  
311 (0.068 mmol/L for 1% of mineral oxidation). However the redox reaction at pH 5 is much faster  
312 than at pH 7, due to the regeneration of the magnetite reducing capacity via  $\text{Fe}(\text{II})_{\text{aq}}$  re-adsorption  
313 and the positively charged mineral surface, and continues until  $\text{Fe}(\text{II})_{\text{aq}}$  is consumed.

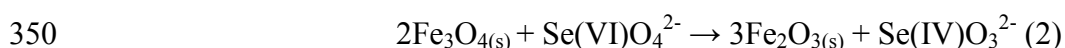
314 **Se(VI) reduction – XAS and STEM**

315 The temporal evolution of the selenium speciation on magnetite in the pH 5 and pH 7  
316 experiments was determined by Se K-edge XANES and EXAFS, using iterative target  
317 transformation factor analysis (ITFA). Both datasets (XANES and EXAFS) were subject to the  
318 ITFA independently, yielding similar results, with relative deviations below 10% (see XANES  
319 and EXAFS results in Figure 3 and Figure 5 and in Tables S4 and S5). Both XANES and  
320 EXAFS spectra collected for selected solid samples from the two experimental series were  
321 successfully fitted with two components: trigonal Se(0) gray and outer-sphere aqueous Se(IV)  
322 (Table S4, Figure 3). The EXAFS data confirm the presence of the gray elemental form (in  
323 contrast to amorphous, red Se(0)), and show even more clearly than XANES the presence of an  
324 oxygen shell indicative of Se(IV). Although the fit gives a good result with the Se(IV) outer-  
325 sphere reference, the low amount of Se(IV) in the samples makes it difficult to ascertain if a  
326 second shell is present. The presence of inner-sphere complexes, as described by Missana et al.  
327 (2009),<sup>30</sup> cannot therefore be excluded. While these two oxidation states have also been reported  
328 as reduction products of selenate by magnetite and green-rust,<sup>20,21</sup> numerous literature examples  
329 show that selenite can be immobilized by iron containing minerals in form of stronger inner-  
330 sphere (creation of covalent or ionic bonds) or/and weaker outer-sphere (electrostatic driven  
331 sorption) complexes, depending on the experimental conditions.<sup>4,11,12,54,55</sup>

332 Initial Se(VI) was not detected on the solids, so all selenate must have been reduced by electrons  
333 from structural Fe(II) in magnetite (at pH 7), or from re-adsorbed Fe(II) (at pH 5); otherwise the  
334 weakly adsorbed Se(VI) would have been removed during filtration.<sup>21</sup>

335 Selenate at pH 7 is only weakly attracted by the mineral surface, even after hypothetical initial  
336 reduction to Se(IV), due to pH conditions close to the isoelectric point of both magnetite and  
337 maghemite surfaces (neutral surface). XANES data fitting showed that in the pH 7 series the  
338 dominating species was gray Se(0) (Figures 3-4), with a small and constant contribution of  
339 Se(IV) (20%) detected between 3 h and 1488 h, but not at 2280 h and 7032 h. The large share of  
340 Se(0) indicates that the main immobilization mechanism at pH 7 followed the reductive  
341 precipitation described by equation (1), with simultaneous oxidation of magnetite to maghemite,  
342 as revealed by Mössbauer data analysis. The presence of the usually soluble Se(IV) species  
343 associated with the solid phase suggests that a small fraction of selenate was reduced only to  
344 selenite at the solid – liquid interface (Se(VI) not detected in solid, Se(IV) not detected in liquid),

345 due to increasing maghemite layer thickness. ICP-AES showed no more Se(VI) uptake after 336  
346 h, so about 30% of maghemite, (equivalent to 3 layers), hindered easy electron transfer. The  
347 Se(IV) stayed adsorbed on the oxidized surface during the first ~1500 h. This secondary  
348 immobilization reaction requires an exchange of only two electrons and no proton consumption  
349 (no Fe(II)<sub>aq</sub> at pH 7):

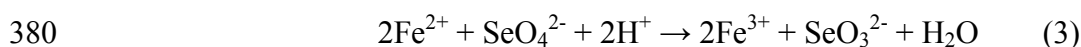


351 At pH 5, the XANES data at 3 h showed only the strong white line of gray Se(0), as a result of  
352 the fast reduction on the magnetite surface (despite the presence of maghemite, due to the acidic  
353 dissolution), which was renewed by Fe(II)<sub>aq</sub> cations being continuously re-adsorbed. This can be  
354 related to a fast Se(VI) drop in solution measured with ICP-AES during the first 336 h (Figure  
355 1). The selenite fraction appeared at 744 h (18%) and stayed nearly constant until 7032 h (15%).

356 Based on these data, we can hypothesize that during the initial phase there is a non-perturbed  
357 electron exchange between magnetite and selenate, assisted by Fe(II)<sub>aq</sub> re-adsorption. As mineral  
358 oxidation is faster than iron re-adsorption, more and more maghemite layers cover the magnetite  
359 core. In this situation, the aqueous iron can only provide a limited number of electrons, which  
360 leads to a partial reduction of selenate to selenite.

361 A monotonic Se(IV) concentration increase reported for solid green rust<sup>20</sup> was attributed to two  
362 parallel reduction processes (selenate to selenite and selenate to elemental selenium). In that  
363 work, the depletion of Fe(II) sites in the vicinity of the adsorption sites prevented the reduction  
364 of the adsorbed selenite to Se(0). In contrast, in our case the aqueous iron renews the mineral  
365 redox activity. As the co-removal ratio shows a linear dependence between 0.17 h and 7032 h,  
366 we assume that the Fe(II)<sub>aq</sub> adsorption site changes as a function of the available reducing sites  
367 on the magnetite surface. In the initial phase, there are many accessible electrons in the system  
368 due to a limited fraction of maghemite. This favors the fast reduction of selenate to Se(0) on the  
369 mineral surface and proton consumption, which increases the pH (equation 1). A small increase  
370 in pH causes re-adsorption of the aqueous iron, as in the absence of selenate.<sup>31</sup> So, here, the  
371 aqueous iron renews the reducing power of the mineral surface, with the re-adsorption being  
372 spread over time, lasting over ~7000 h.

373 In the second phase, iron re-adsorbs on a thicker maghemite layer (faster magnetite electron  
374 consumption than electron donation from Fe(II)<sub>aq</sub>), renewing only partially the reducing capacity  
375 of the mineral (an easy electron exchange with the remaining magnetite core is blocked). So in  
376 this second phase, the reducing power allows only for reduction of selenate to selenite, with the  
377 partially reduced oxyanion being adsorbed to maghemite,<sup>12</sup> in the form of thermodynamically  
378 favored Fe-Se(IV)O<sub>3</sub> species.<sup>30</sup> This reaction theoretically consumes two iron cations per  
379 selenate anion:



381 but the real redox process is more complicated due to the presence of the underlying mineral.

### 382 **Insights into the growth mechanism of Se nanowires**

383 Selected solids from sorption experiments (pH 7: after 0.17 and 2280 h; pH 5: after 0.17, 144,  
384 2280 and 4032 h) were examined with TEM, to probe the shape and size of magnetite particles  
385 and the selenium reaction products. Pure magnetite appeared as a collection of rather spherical  
386 particles with 5-50 nm diameter, which tend to aggregate even after redistribution in the  
387 ultrasonic bath (Figure S2). The pH 5 and 7 samples collected at 0.17 h also showed only  
388 magnetite grains in TEM images - their composition was confirmed by X-ray energy-dispersive  
389 spectroscopy (XEDS, see Figure S3). As XANES analysis showed a clear signal from Se(0) at 3  
390 h (at both pH), the nucleation of reduced selenium species must have occurred between 0.17 h  
391 and 3 h.

392 Finally, the sample collected after 144 h of reaction at pH 5 showed several Se nanowires as  
393 bright elongated areas in the STEM-HAADF image and STEM-XEDS map (Figure 4 a-b),  
394 similar to that observed for goethite/magnetite at pH 8.<sup>20</sup> The largest crystals reached lengths of  
395 ~10 μm and diameters of ~100-200 nm.

396 All the remaining samples showed the development of Se(0) nanowires, which have grown along  
397 the [001] direction (axial direction), while their thickness remained comparable to the ones  
398 observed at 144 h. The examples in Figure 4 c-d, g-h show magnetite reacted with Se(VI) at pH  
399 5 after 4032 h and pH 7 at 2280 h. This preferential one-dimensional Se growth direction along  
400 the [001] axis is typical for gray Se(0) crystals grown in the laboratory.<sup>56,57</sup> Two diffraction  
401 patterns obtained on the particle attached to the wire and at the wire itself (Figure 4 e-f) were in

402 line with trigonal (P3<sub>1</sub>21) gray Se(0).<sup>57</sup> Other forms of reduced selenium species were not  
403 detected.

404 The formation of the Se(0) nanowires within a 3D matrix of magnetite nanoparticles implies  
405 some type of transport of the reduced species from the reducing loci - supposedly close to the  
406 magnetite/water interface - to the tip of the growing nanowires. Two hypotheses can be made  
407 here: (i) growth via an Ostwald ripening process, by which smaller NPs would dissolve to feed  
408 the growth of larger ones – the nanowires. Indeed, smaller precipitates with more rounded shapes  
409 can be observed close to the Se nanowires (Figure 4, c-f); (ii) growth via the oriented attachment  
410 of smaller Se NPs. More experiments are needed, with higher temporal resolution, to ascertain  
411 the precise of growth mechanism of these elemental Se nanowires.

412 Although the evidence for the existence of Se(0) nanowires in STEM-HAADF images is clear, it  
413 may seem contradictory to XRD data, where only a small percentage of the gray form was  
414 detected. This can be explained by an uneven distribution of wires in the magnetite matrix.  
415 Scanning different regions of the TEM grids showed plenty of spots where selenium was not  
416 detectable at all on the STEM-XEDS maps, located close to regions with selenium concentrated  
417 in the form of wires.

418

#### 419 **Environmental relevance**

420 Highly mobile selenate is a concern for the nuclear waste, coal mining and oil refinery industries.  
421 Because of weathering of selenium bearing rocks, such as shales and coal, or by corrosion of  
422 steel canisters used for spent fuel geological storage, this highly toxic element can escape into  
423 the surrounding environment. However in anoxic environments, pore space and corrosion  
424 products often contain Fe(II), which can actively participate in selenate reductive  
425 immobilization. Our study demonstrates that, as opposed to selenate, which is quickly reduced to  
426 Se(IV), selenite has rather slow reduction kinetics, also affected by the limited electron transfer  
427 due to partially oxidized magnetite surfaces. However, the thermodynamically less likely  
428 coincidence of selenite and magnetite is indeed not so unlikely when seen from a kinetic  
429 perspective, and may play an important role not only under nuclear waste repository conditions,  
430 but also for general waste water remediation purposes as those e.g. arising from coal mining  
431 waste waters and other causes of acid mine drainages, or for drinking water purification. The  
432 presence of aqueous Fe(II) stimulates the reduction process, due to the renewed reducing power

433 of the mineral surface. This opens a new way to control selenium concentration in a variety of  
434 critical effluents. This finding is also important in the context of nuclear waste repositories:  
435 aqueous Fe(II) is expected to be formed via the anaerobic corrosion of the steel canister, having  
436 the potential ability to act as a booster of selenium reduction processes.

437 Moreover, our study shows the formation of very anisotropic Se(0) precipitates in the form of  
438 crystalline nanowires. This anisotropy contrasts with the very isotropic distribution of magnetite  
439 nanoparticles, suggesting the transport of reduced species from the site where the reduction takes  
440 place to the tips of the Se nanowires –their growth sites. This implies that the reduced species of  
441 selenium, which are usually considered as non-mobile, show some mobility under these  
442 conditions. The existence of this unknown mechanism for transport of reduced selenium species  
443 has important implication for the safety assessment of technological applications such as the  
444 underground sites for nuclear waste storage. More research is needed to better understand the  
445 transport of these reduced species, whether solid or aqueous, in view of the risk associated with  
446 <sup>79</sup>Se.

447

#### 448 SUPPORTING INFORMATION

449 Results of the ancillary characterization of magnetite nanoparticles and reduced phases of  
450 selenium by XRD, <sup>57</sup>Fe Mössbauer spectrometry, EXAFS and STEM-HAADF / XEDS, the  
451 stabilization of the background electrolyte and the measurements of the redox potential are  
452 presented in the Supporting Information.

#### 453 AUTHOR CONTRIBUTIONS

454 The manuscript was written through contributions of all authors. All authors have given approval  
455 to the final version of the manuscript.

#### 456 FUNDING SOURCES

457 The postdoctoral contract of AP and research grant were funded by the European Joint Program  
458 on Radioactive Waste Management (EURAD - European Union's Horizon 2020, grant  
459 agreement No 847593).

460

#### 461 ACKNOWLEDGMENTS

462 We thank the BM20 and ID31 beamlines at the ESRF for providing in-house beamtime for XAS  
463 and XRD measurements. Funding from the FUTURE WP of the EURAD European project is  
464 acknowledged. Carolina Guida (ISTerre) is thanked for her help with the thermodynamic  
465 calculations for the project.

466

#### 467 ABBREVIATIONS

468 ICP-AES - Inductively Coupled Plasma Atomic Emission Spectroscopy

469 IC – Ion Chromatography

470 STEM – Scanning Transmission Electron Microscopy

471 HAADF - High Angular Angle Dark Field

472 SAED - Selected Area Electron Diffraction

473 XANES – X-ray Absorption Near-Edge Structure

474 EXAFS – Extended X-ray Absorption Fine Structure

475

476

477

478

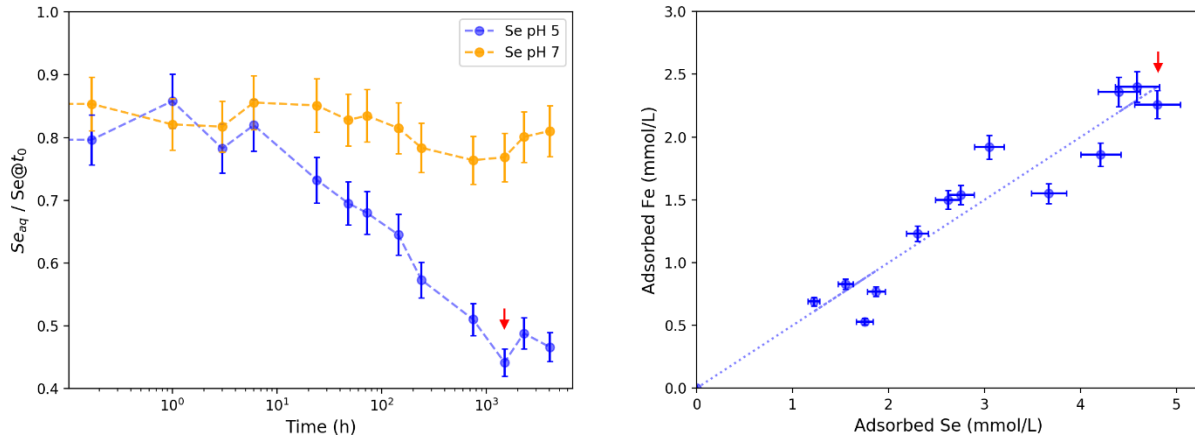
479

480

## FIGURES AND TABLES

481

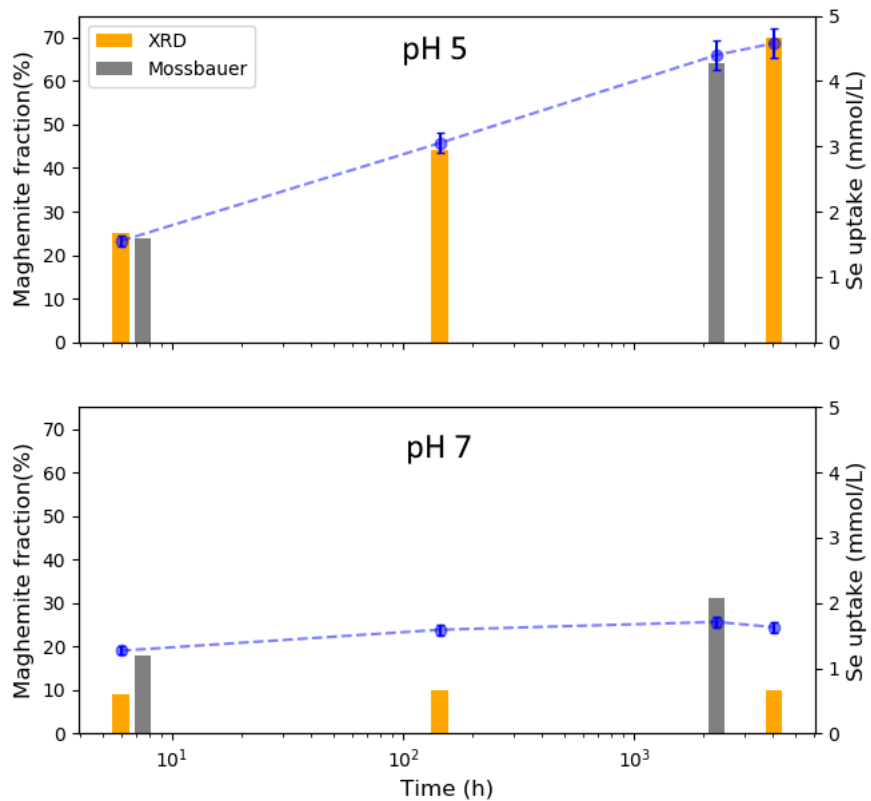
482



483

484 **Figure 1.** (a) Selenium sorption kinetics observed in the two batch experiments. (b) Correlation  
485 between Se sorption and Fe(II) sorption at pH 5. The red arrow indicates the time of nearly  
486 complete adsorption of Fe(II) in the pH 5 experiment. Error bars represent 5% error of the ICP-  
487 AES measurements.

488



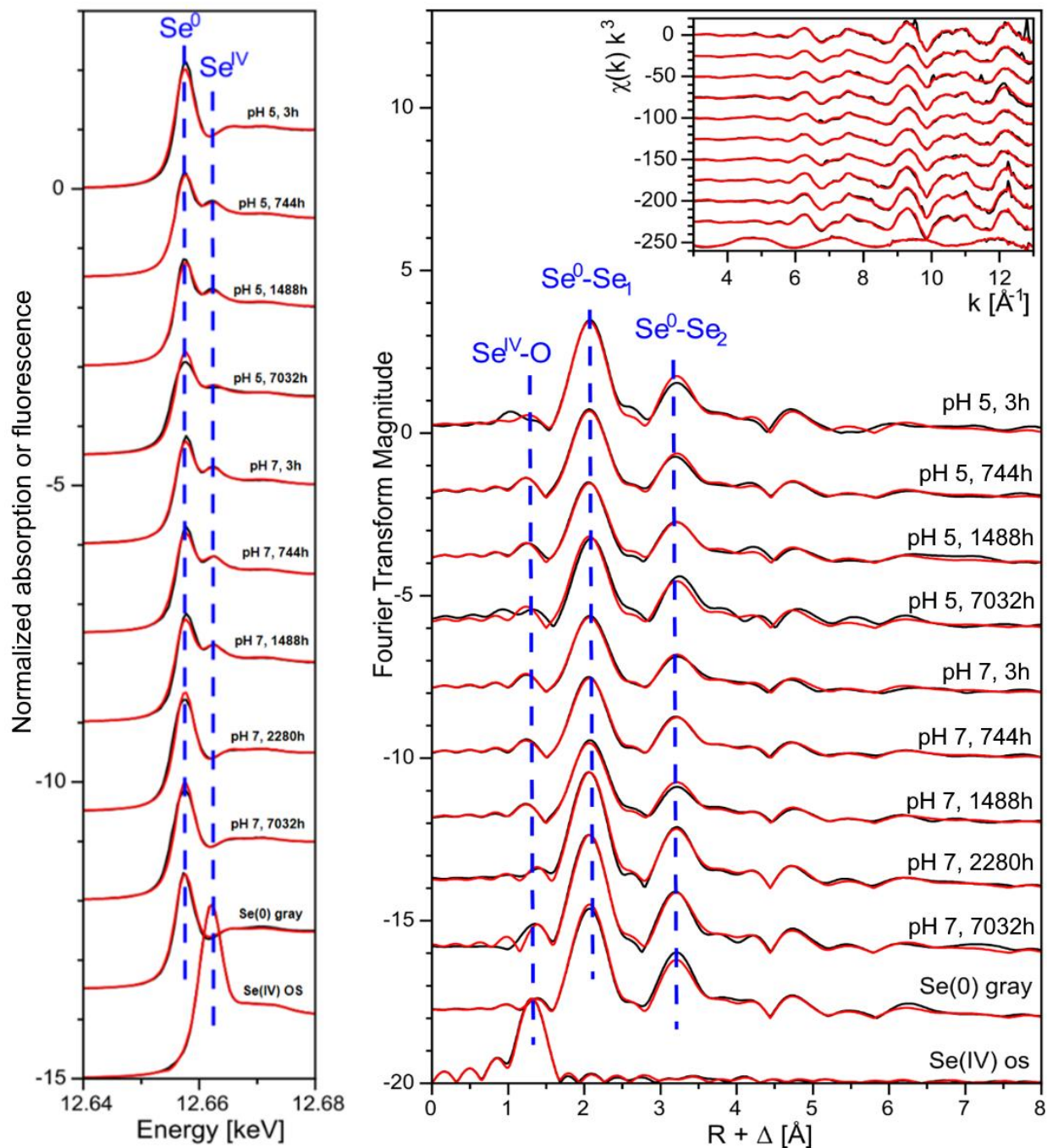
490

491 **Figure 2.** Degree of magnetite to maghemite conversion from Mössbauer at 77 K (gray bars) and  
 492 XRD pattern modeling (orange bars), in comparison to selenium uptake (blue circles). Error bars  
 493 represent 5% error of the ICP-AES measurements.

494

495

496

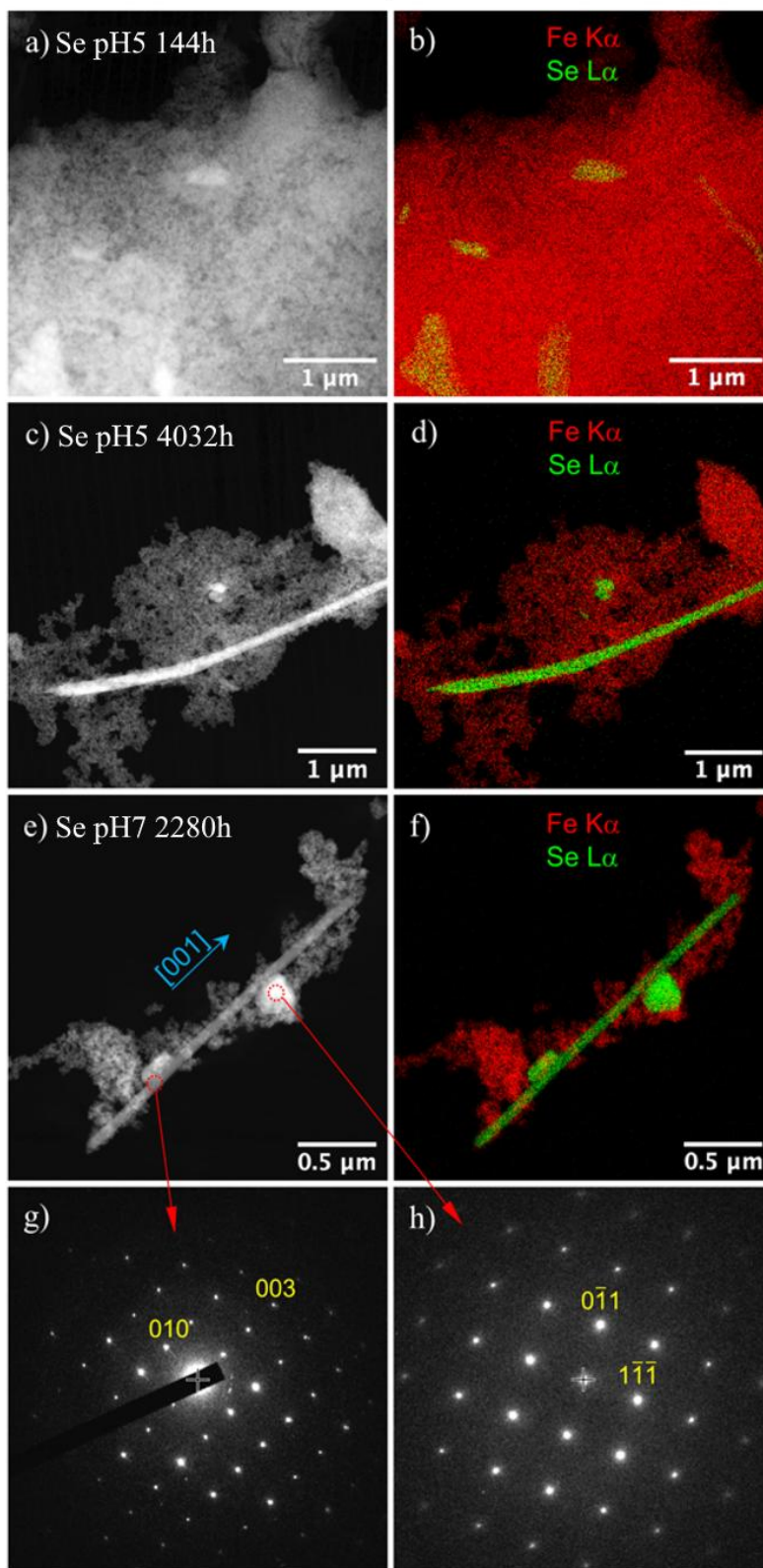


497

498 **Figure 3.** Selenium K-edge XANES (left) and EXAFS (right) spectra of the two time series of  
 499 Se(VI) experiments at pH 5 and 7, and the two standard spectra (gray Se(0) and Se(IV) outer  
 500 sphere sorption complexes (OS)). Inset: Right: Black lines – experimental data, red lines:  
 501 reconstruction by two components.

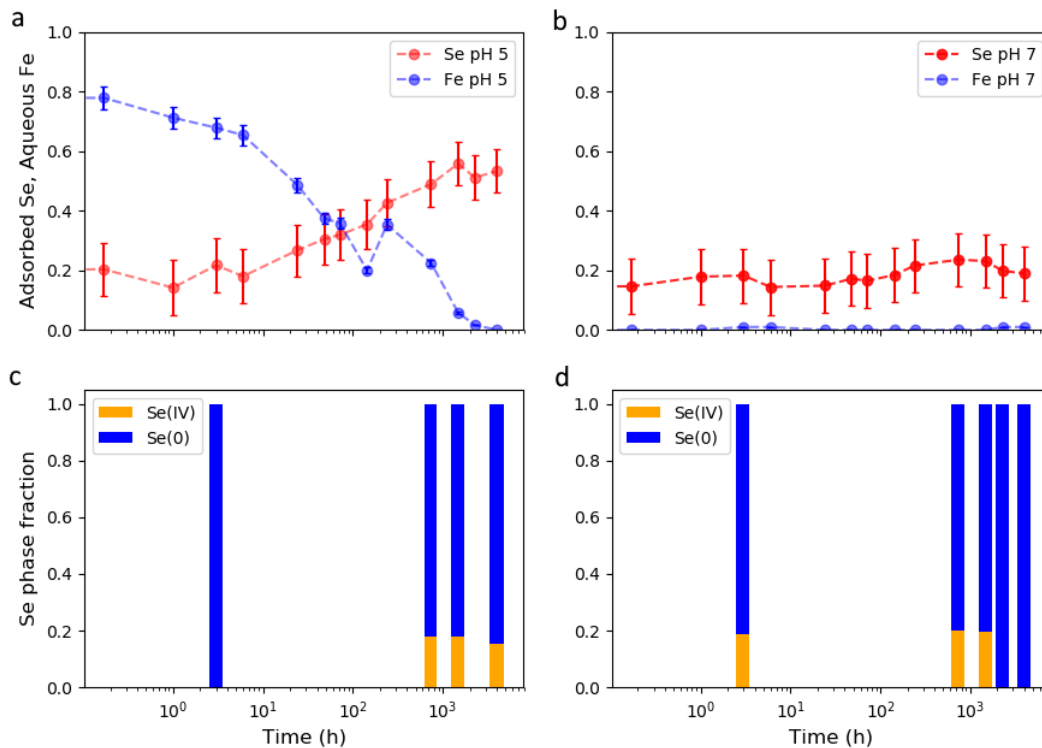
502

# STEM-HAADF, STEM-HEDX



504 **Figure 4.** STEM-HAADF images (a, c, e) and STEM-XEDS maps (b, d, f) of magnetite-Se  
 505 samples: (a) and (b) show results from the experiments at pH 5 after 144 h, where several crystal  
 506 seeds of reduced selenium are observed; (c) and (d) show the last time (4032 h) of the  
 507 experiment at pH 5, where  $\sim 5 \mu\text{m}$  long selenium nanowire are observed ; (e) and (f) show results  
 508 of the pH 7 experiment at 2280 h, where  $\sim 2.5 \mu\text{m}$  long elemental selenium nanowires can be  
 509 observed together with small selenium seeds; (g) shows the zone-axis pattern along the [100]  
 510 direction of the  $\text{P3}_121 \text{ Se}(0)$  structure; (h) electron diffraction patterns along the [211] direction  
 511 of the  $\text{P3}_121 \text{ Se}(0)$  structure.

512



513

514 **Figure 5.** Fraction of aqueous Fe (blue) and adsorbed Se (red) at pH 5 (a) and pH 7 (b).  
 515 Fractions of Se(0) and Se(IV) associated with the solid phase at pH 5 (c) and pH 7 (d).

516

517

## 518 REFERENCES

- 519 (1) Levander, O. A.; Burk, R. F.; Hatfield, D. L.; Berry, M. J.; Gladyshev, V. N. Update of  
520 Human Dietary Standards for Selenium. In *Selenium. Its Molecular Biology and Role in*  
521 *Human Health*; Springer US: New York, 2006; Vol. 1, pp 399–410.
- 522 (2) Stolz, J. E.; Basu, P.; Santini, J. M.; Oremland, R. S. Arsenic and Selenium in Microbial  
523 Metabolism. *Annu. Rev. Microbiol.* **2006**, *60*, 107–130.  
524 <https://doi.org/10.1146/annurev.micro.60.080805.142053>.
- 525 (3) Gebreyessus, G. D.; Zewge, F. A Review on Environmental Selenium Issues. *SN Applied*  
526 *Sciences*. 2019. <https://doi.org/10.1007/s42452-018-0032-9>.
- 527 (4) Fernández-Martínez, A.; Charlet, L. Selenium Environmental Cycling and Bioavailability:  
528 A Structural Chemist Point of View. *Reviews in Environmental Science and*  
529 *Biotechnology*. 2009, pp 81–110. <https://doi.org/10.1007/s11157-009-9145-3>.
- 530 (5) He, Y.; Xiang, Y.; Zhou, Y.; Yang, Y.; Zhang, J.; Huang, H.; Shang, C.; Luo, L.; Gao, J.;  
531 Tang, L. Selenium Contamination, Consequences and Remediation Techniques in Water  
532 and Soils: A Review. *Environmental Research*. 2018.  
533 <https://doi.org/10.1016/j.envres.2018.02.037>.
- 534 (6) Curti, E.; Puranen, A.; Grolimund, D.; Jädernas, D.; Sheptyakov, D.; Mesbah, A.  
535 Characterization of Selenium in UO<sub>2</sub> Spent Nuclear Fuel by Micro X-Ray Absorption  
536 Spectroscopy and Its Thermodynamic Stability. *Environ. Sci. Process. Impacts* **2015**, *17*  
537 (10). <https://doi.org/10.1039/c5em00275c>.
- 538 (7) ANDRA. Dossier 2005 Argile. Evaluation de Surete Du Stockage Geologique. Agence  
539 National pour la gestion des Dechets Radioactifs: Paris 2005.
- 540 (8) Rojo, H.; Scheinost, A. C.; Lothenbach, B.; Laube, A.; Wieland, E.; Tits, J. Retention of  
541 Selenium by Calcium Aluminate Hydrate (AFm) Phases under Strongly-Reducing  
542 Radioactive Waste Repository Conditions. *Dalt. Trans.* **2018**, *47* (12).  
543 <https://doi.org/10.1039/c7dt04824f>.
- 544 (9) Ma, B.; Fernandez-Martinez, A.; Grangeon, S.; Tournassat, C.; Findling, N.; Carrero, S.;  
545 Tisserand, D.; Bureau, S.; Elkaïm, E.; Marini, C.; et al. Selenite Uptake by Ca–Al LDH: A  
546 Description of Intercalated Anion Coordination Geometries. *Environ. Sci. Technol.* **2018**,  
547 *52* (3), 1624–1632. <https://doi.org/10.1021/acs.est.7b04644>.
- 548 (10) Aimoz, L.; Wieland, E.; Taviot-Guého, C.; Dähn, R.; Vespa, M.; Churakov, S. V.

- 549 Structural Insight into Iodide Uptake by AFm Phases. *Environ. Sci. Technol.* **2012**, *46* (7),  
550 3874–3881. <https://doi.org/10.1021/es204470e>.
- 551 (11) Jordan, N.; Ritter, A.; Foerstendorf, H.; Scheinost, A. C.; Weiß, S.; Heim, K.; Grenzer, J.;  
552 Mücklich, A.; Reuther, H. Adsorption Mechanism of Selenium(VI) onto Maghemite.  
553 *Geochim. Cosmochim. Acta* **2013**, *103*. <https://doi.org/10.1016/j.gca.2012.09.048>.
- 554 (12) Jordan, N.; Ritter, A.; Scheinost, A. C.; Weiss, S.; Schild, D.; Hübner, R. Selenium(IV)  
555 Uptake by Maghemite ( $\gamma$ -Fe<sub>2</sub>O<sub>3</sub>). *Environ. Sci. Technol.* **2014**, *48* (3), 1665–1674.  
556 <https://doi.org/10.1021/es4045852>.
- 557 (13) Jordan, N.; Lomenech, C.; Marmier, N.; Giffaut, E.; Ehrhardt, J. J. Sorption of  
558 Selenium(IV) onto Magnetite in the Presence of Silicic Acid. *J. Colloid Interface Sci.*  
559 **2009**, *329* (1), 17–23. <https://doi.org/10.1016/j.jcis.2008.09.052>.
- 560 (14) Ma, B.; Charlet, L.; Fernandez-Martinez, A.; Kang, M.; Madé, B. A Review of the  
561 Retention Mechanisms of Redox-Sensitive Radionuclides in Multi-Barrier Systems. *Appl.*  
562 *Geochemistry* **2019**, *100*. <https://doi.org/10.1016/j.apgeochem.2018.12.001>.
- 563 (15) Scheinost, A. C.; Charlet, L. Selenite Reduction by Mackinawite, Magnetite and Siderite:  
564 XAS Characterization of Nanosized Redox Products. *Environ. Sci. Technol.* **2008**, *42* (6),  
565 1984–1989. <https://doi.org/10.1021/es071573f>.
- 566 (16) Ma, B.; Fernandez-Martinez, A.; Kang, M.; Wang, K.; Lewis, A. R.; Maffei, T. G. G.;  
567 Findling, N.; Salas-Colera, E.; Tisserand, D.; Bureau, S.; et al. Influence of Surface  
568 Compositions on the Reactivity of Pyrite toward Aqueous U(VI). *Environ. Sci. Technol.*  
569 **2020**, *54* (13). <https://doi.org/10.1021/acs.est.0c01854>.
- 570 (17) Qafoku, O.; Pearce, C. I.; Neumann, A.; Kovarik, L.; Zhu, M.; Ilton, E. S.; Bowden, M.  
571 E.; Resch, C. T.; Arey, B. W.; Arenholz, E.; et al. Tc(VII) and Cr(VI) Interaction with  
572 Naturally Reduced Ferruginous Smectite from a Redox Transition Zone. *Environ. Sci.*  
573 *Technol.* **2017**, *51* (16), 9042–9052. <https://doi.org/10.1021/acs.est.7b02191>.
- 574 (18) Myneni, S. C. B.; Tokunaga, T. K.; Brown, G. E. Abiotic Selenium Redox  
575 Transformations in the Presence of Fe(II,III) Oxides. *Science* (80-. ). **1997**, *278* (5340),  
576 1106–1109.
- 577 (19) Scheidegger, A. M.; Grolimund, D.; Cui, D.; Devoy, J.; Spahiu, K.; Wersin, P.; Bonhoure,  
578 I.; Janousch, M. Reduction of Selenite on Iron Surfaces: A Micro-Spectroscopic Study. *J.*  
579 *Phys. Iv* **2003**, *104*, 417–420.

- 580 (20) Onoguchi, A.; Granata, G.; Haraguchi, D.; Hayashi, H.; Tokoro, C. Kinetics and  
581 Mechanism of Selenate and Selenite Removal in Solution by Green Rust-Sulfate. *R. Soc.*  
582 *Open Sci.* **2019**, *6* (4). <https://doi.org/10.1098/rsos.182147>.
- 583 (21) Goberna-Ferrón, S.; Asta, M. P.; Zareepolgardani, B.; Bureau, S.; Findling, N.;  
584 Simonelli, L.; Greneche, J. M.; Charlet, L.; Fernandez-Martínez, A. Influence of Silica  
585 Coatings on Magnetite-Catalyzed Selenium Reduction. *Environ. Sci. Technol.* **2021**, *55*  
586 (5). <https://doi.org/10.1021/acs.est.0c08146>.
- 587 (22) Martínez, M.; Giménez, J.; De Pablo, J.; Rovira, M.; Duro, L. Sorption of Selenium(IV)  
588 and Selenium(VI) onto Magnetite. *Appl. Surf. Sci.* **2006**, *252* (10), 3767–3773.  
589 <https://doi.org/10.1016/j.apsusc.2005.05.067>.
- 590 (23) Curti, E.; Aimoz, L.; Kitamura, A. Selenium Uptake onto Natural Pyrite. *J. Radioanal.*  
591 *Nucl. Chem.* **2013**, *295* (3). <https://doi.org/10.1007/s10967-012-1966-9>.
- 592 (24) Breynaert, E.; Scheinost, A. C.; Dom, D.; Rossberg, A.; Vancluysen, J.; Gobechiya, E.;  
593 Kirschhock, C. E. A.; Maes, A. Reduction of Se(IV) in Boom Clay: XAS Solid Phase  
594 Speciation. *Environ. Sci. Technol.* **2010**, *44* (17). <https://doi.org/10.1021/es100569e>.
- 595 (25) Breynaert, E.; Bruggeman, C.; Maes, A. XANES-EXAFS Analysis of Se Solid-Phase  
596 Reaction Products Formed upon Contacting Se(IV) with FeS<sub>2</sub> and FeS. *Environ. Sci.*  
597 *Technol.* **2008**, *42* (10), 3595–3601. <https://doi.org/10.1021/es071370r>.
- 598 (26) Das, S.; Lindsay, M. B. J.; Essilfie-Dughan, J.; Hendry, M. J. Dissolved Selenium(VI)  
599 Removal by Zero-Valent Iron under Oxic Conditions: Influence of Sulfate and Nitrate.  
600 *ACS Omega* **2017**, *2* (4). <https://doi.org/10.1021/acsomega.6b00382>.
- 601 (27) Scheinost, A. C.; Kirsch, R.; Banerjee, D.; Fernandez-Martinez, A.; Zaenker, H.; Funke,  
602 H.; Charlet, L. X-Ray Absorption and Photoelectron Spectroscopy Investigation of  
603 Selenite Reduction by Fe-II-Bearing Minerals. *J. Contam. Hydrol.* **2008**, *102* (3–4), 228–  
604 245. <https://doi.org/10.1016/j.jconhyd.2008.09.018>.
- 605 (28) Börsig, N.; Scheinost, A. C.; Schild, D.; Neumann, T. Mechanisms of Selenium Removal  
606 by Partially Oxidized Magnetite Nanoparticles for Wastewater Remediation. *Appl.*  
607 *Geochemistry* **2021**, *132*, 105062. <https://doi.org/10.1016/j.apgeochem.2021.105062>.
- 608 (29) Kim, S. S.; Min, J. H.; Lee, J. K.; Baik, M. H.; Choi, J. W.; Shin, H. S. Effects of PH and  
609 Anions on the Sorption of Selenium Ions onto Magnetite. *J. Environ. Radioact.* **2012**, *104*  
610 (1), 1–6. <https://doi.org/10.1016/j.jenvrad.2011.09.013>.

- 611 (30) Missana, T.; Alonso, U.; Scheinost, A. C.; Granizo, N.; Garcia-Gutierrez, M. Selenite  
612 Retention by Nanocrystalline Magnetite: Role of Adsorption, Reduction and  
613 Dissolution/Co-Precipitation Processes. *Geochim. Cosmochim. Acta* **2009**, *73* (20), 6205–  
614 6217. <https://doi.org/10.1016/j.gca.2009.07.005>.
- 615 (31) Peng, H.; Pearce, C. I.; Huang, W.; Zhu, Z.; N'Diaye, A. T.; Rosso, K. M.; Liu, J.  
616 Reversible Fe(II) Uptake/Release by Magnetite Nanoparticles. *Environ. Sci. Nano* **2018**, *5*  
617 (7). <https://doi.org/10.1039/c8en00328a>.
- 618 (32) Li, Y.; Li, Y.; Li, Y.; Wei, G.; Wei, G.; Liang, X.; Liang, X.; Liang, X.; Zhang, C.; Zhu,  
619 J.; et al. Metal Substitution-Induced Reducing Capacity of Magnetite Coupled with  
620 Aqueous Fe(II). *ACS Earth Sp. Chem.* **2020**, *4* (6).  
621 <https://doi.org/10.1021/acsearthspacechem.0c00089>.
- 622 (33) Gubler, R.; ThomasArrigo, L. K. Ferrous Iron Enhances Arsenic Sorption and Oxidation  
623 by Non-Stoichiometric Magnetite and Maghemite. *J. Hazard. Mater.* **2021**, *402*.  
624 <https://doi.org/10.1016/j.jhazmat.2020.123425>.
- 625 (34) Gorski, C. A.; Handler, R. M.; Beard, B. L.; Pasakarnis, T.; Johnson, C. M.; Scherer, M.  
626 M. Fe Atom Exchange between Aqueous Fe<sup>2+</sup> and Magnetite. *Environ. Sci. Technol.*  
627 **2012**, *46* (22), 12399–12407. <https://doi.org/10.1021/es204649a>.
- 628 (35) Jolivet, J. P.; Belleville, P.; Tronc, E.; Livage, J. Influence of Fe(II) on the Formation of  
629 the Spinel Iron Oxide in Alkaline Medium. *Clays Clay Miner.* **1992**, *40* (5).  
630 <https://doi.org/10.1346/CCMN.1992.0400506>.
- 631 (36) Kieffer, J.; Karkoulis, D. PyFAI, a Versatile Library for Azimuthal Regrouping. In  
632 *Journal of Physics: Conference Series*; 2013; Vol. 425. [https://doi.org/10.1088/1742-](https://doi.org/10.1088/1742-6596/425/20/202012)  
633 [6596/425/20/202012](https://doi.org/10.1088/1742-6596/425/20/202012).
- 634 (37) Rodriguez-Carvajal, J. Recent Advances in Magnetic Structure Determination by Neutron  
635 Powder Diffraction. *Phys. B* **1993**, *192*, 55. [https://doi.org/10.1016/0921-4526\(93\)90108-](https://doi.org/10.1016/0921-4526(93)90108-I)  
636 [I](https://doi.org/10.1016/0921-4526(93)90108-I).
- 637 (38) Teillet, J.; Varret, F. unpublished MOSFIT program, Université Le Mans, Le Mans,  
638 France.
- 639 (39) Abramoff, M. D.; Magalhães, P. J.; Ram, S. J. Image Processing with ImageJ.  
640 *Biophotonics International*. 2004. <https://doi.org/10.1201/9781420005615.ax4>.
- 641 (40) Palmer, D. C. SingleCrystal 4: Real-Time Multi-Phase Diffraction Simulation. *Journal of*

- 642 *Applied Crystallography*. International Union of Crystallography June 1, 2020, p 860.  
643 <https://doi.org/10.1107/S1600576720006378>.
- 644 (41) Wechsler, B. A.; Lindsley, D. H.; Prewitt, C. T. Crystal Structure and Cation Distribution  
645 in Titanomagnetites (Fe<sub>3</sub>-XTi<sub>x</sub>O<sub>4</sub>). *Am. Mineral.* **1984**, *69* (7–8), 754–770.
- 646 (42) Scheinost, A. C.; Claussner, J.; Exner, J.; Feig, M.; Findeisen, S.; Hennig, C.; Kvashnina,  
647 K. O.; Naudet, D.; Prieur, D.; Rossberg, A.; et al. ROBL-II at ESRF: A Synchrotron  
648 Toolbox for Actinide Research. *J. Synchrotron Radiat.* **2021**, *28*.  
649 <https://doi.org/10.1107/S1600577520014265>.
- 650 (43) Webb, S. M. SIXpack: A Graphical User Interface for XAS Analysis Using IFEFFIT.  
651 *Phys. Scr. T* **2005**, *T115*. <https://doi.org/10.1238/Physica.Topical.115a01011>.
- 652 (44) Ressler, T. WinXAS: A Program for X-Ray Absorption Spectroscopy Data Analysis  
653 under MS-Windows. *J. Synchrotron Radiat.* **1998**, *5*, 118–122.
- 654 (45) Roßberg, A.; Reich, T.; Bernhard, G. Complexation of Uranium(VI) with Protocatechuic  
655 Acid-Application of Iterative Transformation Factor Analysis to EXAFS Spectroscopy.  
656 *Anal. Bioanal. Chem.* **2003**, *376* (5). <https://doi.org/10.1007/s00216-003-1963-5>.
- 657 (46) Yalçintaş, E.; Scheinost, A. C.; Gaona, X.; Altmaier, M. Systematic XAS Study on the  
658 Reduction and Uptake of Tc by Magnetite and Mackinawite. *Dalt. Trans.* **2016**, *45* (44).  
659 <https://doi.org/10.1039/c6dt02872a>.
- 660 (47) Charlet, L.; Scheinost, A. C.; Tournassat, C.; Greneche, J. M.; Gehin, A.; Fernandez-  
661 Martinez, A.; Coudert, S.; Tisserand, D.; Brendle, J. Electron Transfer at the  
662 Mineral/Water Interface: Selenium Reduction by Ferrous Iron Sorbed on Clay. *Geochim.*  
663 *Cosmochim. Acta* **2007**, *71* (23), 5731–5749.
- 664 (48) Kim, S. S.; Min, J. H.; Lee, J. K.; Baik, M. H.; Choi, J. W.; Shin, H. S. Effects of PH and  
665 Anions on the Sorption of Selenium Ions onto Magnetite. *J. Environ. Radioact.* **2012**, *104*  
666 (1), 1–6. <https://doi.org/10.1016/j.jenvrad.2011.09.013>.
- 667 (49) Klausen, J.; Tröber, S. P.; Haderlein, S. B.; Schwarzenbach, R. P. Reduction of  
668 Substituted Nitrobenzenes by Fe (II) in Aqueous Mineral Suspensions. *Environ. Sci.*  
669 *Technol.* **1995**, *29* (9). <https://doi.org/10.1021/es00009a036>.
- 670 (50) Tronc, E.; Jolivet, J. P. EXCHANGE AND REDOX REACTIONS AT THE  
671 INTERFACE OF SPINEL-LIKE IRON OXIDE COLLOIDS IN SOLUTION: FE(II)  
672 ADSORPTION. *Adsorpt. Sci. Technol.* **1984**, *1* (3).

- 673 <https://doi.org/10.1177/026361748400100307>.
- 674 (51) Yoon, I. H.; Bang, S.; Kim, K. W.; Kim, M. G.; Park, S. Y.; Choi, W. K. Selenate  
675 Removal by Zero-Valent Iron in Oxidic Condition: The Role of Fe(II) and Selenate  
676 Removal Mechanism. *Environ. Sci. Pollut. Res.* **2016**, *23* (2).  
677 <https://doi.org/10.1007/s11356-015-4578-4>.
- 678 (52) Fraga-García, P.; Schwaminger, S. P.; Berensmeier, S.; Bauer, D.; Wagner, F. E.  
679 Oxidation of Magnetite Nanoparticles: Impact on Surface and Crystal Properties.  
680 *CrystEngComm* **2016**, *19* (2), 246–255. <https://doi.org/10.1039/c6ce02421a>.
- 681 (53) Cherin, P.; Unger, P. The Crystal Structure of Trigonal Selenium. *Inorganic Chemistry*.  
682 1967. <https://doi.org/10.1021/ic50054a037>.
- 683 (54) Peng, H.; Pearce, C. I.; N'Diaye, A. T.; Zhu, Z.; Ni, J.; Rosso, K. M.; Liu, J.  
684 Redistribution of Electron Equivalents between Magnetite and Aqueous Fe<sup>2+</sup> Induced by  
685 a Model Quinone Compound AQDS. *Environ. Sci. Technol.* **2019**.  
686 <https://doi.org/10.1021/acs.est.8b05098>.
- 687 (55) Ma, B.; Fernandez-Martinez, A.; Wang, K.; Madé, B.; Hénocq, P.; Tisserand, D.; Bureau,  
688 S.; Charlet, L. Selenite Sorption on Hydrated CEM-V/A Cement in the Presence of Steel  
689 Corrosion Products: Redox vs Nonredox Sorption. *Environ. Sci. Technol.* **2020**, *54* (4),  
690 2344–2352. <https://doi.org/10.1021/acs.est.9b06876>.
- 691 (56) Sinha, A. K.; Sasmal, A. K.; Mehetor, S. K.; Pradhan, M.; Pal, T. Evolution of  
692 Amorphous Selenium Nanoballs in Silicone Oil and Their Solvent Induced Morphological  
693 Transformation. *Chem. Commun.* **2014**, *50* (99). <https://doi.org/10.1039/c4cc08168d>.
- 694 (57) Xiong, S.; Xi, B.; Wang, W.; Wang, C.; Fei, L.; Zhou, H.; Qian, Y. The Fabrication and  
695 Characterization of Single-Crystalline Selenium Nanoneedles. *Cryst. Growth Des.* **2006**, *6*  
696 (7). <https://doi.org/10.1021/cg060005t>.

697

698